Internal tides near the Celtic Sea shelf break: a new look at a well known problem

Vasiliy Vlasenko[a], Nataliya Stashchuk[a],

[a]*School of Marine Science and Engineering, University of Plymouth, Drake Circus, Plymouth, PL4 8AA, UK*

Abstract

Internal waves generated by tides in the Celtic Sea were investigated on the basis of in-situ data collected at the continental slope in July 2012, and theoretically using a weakly nonlinear theory and the Massachusetts Institute of Technology general circulation model. It was found that internal solitary waves generated over the shelf break and propagated seaward did not survive in the course of their evolution. Due to the large bottom steepness they disintegrated locally over the continental slope radiating several wave systems seaward and transforming their energy to higher baroclinic modes. In the open part of the sea, i.e. 120 km away from the shelf break, internal waves were generated by a baroclinic tidal beam which was radiated from the shelf break downward to the abyss. After reflection from the bottom it returned back to the surface where it hit the seasonal pycnocline and generated packets of high-mode internal solitary waves. Another effect that had strong implications for the wave dynamics was internal wave reflection from sharp changes of vertical fluid stratification in the main pycnocline. A large proportion of the tidal beam energy that propagated downward did not reach the bottom but reflected upward from the layered pycnocline and

returned back to the surface seasonal pycnocline where it generated some extra higher mode internal wave systems, including internal wave breathers.

Key words: Baroclinic tides, internal solitary waves, the Celtic Sea

1. Introduction and motivation

The Celtic Sea (CS) shelf break is one of the "hot spots" of the global ocean where barotropic tidal energy is converted into a baroclinic component (Baines, 1982) making a great contribution to the sustainability of the meridional overturning circulation. This is the reason why much attention is focussed on this site with the aim of quantifying baroclinic processes that develop there. The earliest works by Pingree and Mardell (1981, 1985) followed by more recent studies (Pingree and New, 1995; Holt and Thorpe, 1997; Huthnance et al., 2001; Hopkins et al., 2012) reported the characteristics of internal waves generated by tides over the Celtic Sea shelf break.

The most recent observations were conducted on the 376-th cruise of the RRS "Discovery" (hereafter D376) in June 2012 in the slope-shelf area. The task of the cruise was to quantify the cross shelf transport on the NE Atlantic Ocean margin. In doing so, several long-term moorings with thermistor chains and ADCPs were deployed in the area (some of them are shown in Fig.1), accompanied by CTD surveys and glider missions.

The data collected in-situ revealed evidence of a strong semi-diurnal baroclinic tidal signal that was accompanied by packets of short-period internal solitary waves with amplitudes up to $100\,$m. A detailed analysis of the characteristics of these waves, their spatial structure and dynamics was reported by Vlasenko et al. (2014) who replicated the generated wave fields numerically

2

using the Massachusetts Institute of Technology general circulation model (MITgcm). The model results were validated against the observational data collected during the D376 cruise.

Two classes of tidally generated internal waves were identified in the area with highly corrugated topography shown in Fig.1. Spiral-type internal waves similar to those typical for isolated underwater banks were generated over the headland. The other type was a system of quasi-planar internal wave packets that were generated in the area of several canyons. The spatial structure of these two wave systems is shown in Fig.1 a (see Vlasenko et al. (2014) for more details). Note that the water stratification during the experiment was characterised by a relatively sharp interface at the depth of 50 m and less pronounced main pycnocline located between 500 and 1200 metres (Fig.2 a).

Vlasenko et al. (2014) concluded that the strongest internal wave system is a superposition of a 20 m amplitude semi-diurnal baroclinic tidal wave and a series of internal solitary waves (ISW). These waves were generated over the top of the headland (just in the place of the mooring ST2 deployed at isobath 185 m, see Fig.1 a) and radiated to the shelf and to the deep water towards mooring ST1. The isotherm time series, Fig.3 a, shows the vertical structure of the internal waves recorded at mooring ST1, and Fig.3 b represents a 5-hour fragment with the strongest leading ISW of 105 m amplitude.

The normalized vertical profile of the largest ISW recorded at mooring ST1 is shown in Fig.3 c. It was built by calculation of the displacement of the chosen isotherm from its equilibrium depth before the ISW arrival and normalized by the wave amplitude. Fig.3 c shows that the wave profile reveals the properties of the second baroclinic mode that produces counter-phase

3

displacements of isotherms in the surface and bottom layers. To get a more statistically justified result on the possible appearance of second-mode ISWs at mooring ST1, another 45 of the largest ISWs, with amplitudes larger than 30 m, were analysed in a similar way. Considering the whole cluster of the dots together it was expected to find a general tendency of their distribution that is noise free and statistically significant. It is clear from Fig.3 d that all ISWs are waves of depression in the surface 120 m layer. Below this depth the dots are randomly distributed across the whole range between -1 and 1, so that both the waves of depression and elevation were equally observed.

To make the point clearer, the eigenfunctions of the boundary value problem (BVP)

$$\frac{d^2\Phi}{dz^2} + \frac{N^2(z)}{c_i^2}\Phi = 0, \quad \Phi(0) = \Phi(-H) = 0. \tag{1}$$

were calculated. Here $\Phi(z)$ is the vertical modal structure function, c_i is the phase speed of the $i-$th mode, $N(z)$ is the buoyancy frequency shown in Fig.1 d, H is the water depth.

Two first eigenfunctions of the BVP (1) are presented in Fig.3 d. It is clear that the vertical structure of the ISWs recorded at ST1 does not fit either the first or the second baroclinic mode. However, initially at the place of their generation (in the area of the mooring ST2, see Fig.1), the internal waves had the structure of the first baroclinic mode (for the details see Vlasenko et al. (2014)). Thus, it is unclear what happened to these waves on their way from shallow mooring ST2 to the deeper ST1 , i.e. in the course of their seaward propagation (hereafter, "antishoaling"). What is the ultimate fate of the waves generated on the CS slope: Do they dissipate locally or radiate far away from the place of generation? These fundamental questions on the

mechanisms of the tidal energy conversion and its dissipation were a strong motivation for the present study.

The paper is organized as follows. Section 2 describes the antishoaling process of ISWs in terms of a weakly nonlinear theory and using fine-resolution modelling based on a 2D version of the MITgcm. Section 3 summarises the finding from the antishoaling study and formulates some further questions to be answered. Section 4 reports results of a high-resolution modelling of baroclinic tides in the area. Section 5 outlines the main findings.

2. Does the antishoaling kills all ISWs?

2.1. Weakly nonlinear analysis

Evolution of seaward propagating first mode ISW can be investigated in terms of the Gardner equation:

$$\frac{\partial \eta}{\partial t} + (\alpha \eta + \alpha_1 \eta^2)\frac{\partial \eta}{\partial x} + \beta \frac{\partial^3 \eta}{\partial x^3} = 0. \tag{2}$$

Here η is the displacement of the isopycnals; x is the spatial variable in the direction of wave propagation, and t is the time; α and α_1 are the coefficients of quadratic and cubic non-linearities, respectively; β is the coefficient of dispersion. Note that α, α_1, and β depend on the water depth and stratification as follows (Grimshaw et al., 1997):

$$\alpha = \frac{3c}{2}\frac{\int_{-H}^{0}\left(\frac{d\Phi}{dz}\right)^3 dz}{\int_{-H}^{0}\left(\frac{d\Phi}{dz}\right)^2 dz}, \quad \beta = \frac{c}{2}\frac{\int_{-H}^{0}\Phi^2 dz}{\int_{-H}^{0}\left(\frac{d\Phi}{dz}\right)^2 dz},$$

$$\alpha_1 = \frac{3}{2c}\frac{\int_{-H}^{0}\left\{c^2\left[3\frac{dT}{dz} - 2\left(\frac{d\Phi}{dz}\right)^2\right]\left(\frac{d\Phi}{dz}\right)^2 - \alpha^2\left(\frac{d\Phi}{dz}\right)^2 + \alpha c\left[5\left(\frac{d\Phi}{dz}\right)^2 - 4\frac{dT}{dz}\right]\frac{d\Phi}{dz}\right\} dz}{\int_{-H}^{0}\left(\frac{d\Phi}{dz}\right)^2 dz}.$$

5

Here $\Phi = \Phi_1$ and $c = c_1$ are defined from the BVP (1), T is a normalized solution of the following boundary value problem

$$c\frac{d^2T}{dz^2} + N^2(z)T = -\alpha c\frac{d^2\Phi}{dz^2} + \frac{3c}{2}\frac{d}{dz}\left[\left(\frac{d\Phi}{dz}\right)^2\right], \qquad (3)$$

$$T(0) = T(-H) = 0, \qquad (4)$$

The steady state solutions of the Gardner equation (2) depend on the sign of the coefficients α and α_1. Fig.4 shows the dependence of the coefficients α (red line) and α_1 (blue line) from depth H. It is clear that in the near-shore zone (shalower than 2 km) the coefficient of the quadratic nonlinearity α changes its sign twice. The coefficient of the cubic nonlinearity α_1 is positive on the shelf but negative over the slope deeper than 1260 m.

In the shallow water zone where $H \leq$ 850 m, $\alpha < 0$ and $\alpha_1 > 0$, and according to (Grimshaw et al., 1999, 2004) either negative algebraic solitons or breathers are allowed. For the depth 850 m$< H <$1270 m both coefficients are positive, and the weakly nonlinear theory predicts the existence of either positive algebraic solitons or breathers. Moving further offshore to depths 1270 m$< H <$1750 m the coefficient of the cubic nonlinearity changes its sign again, Fig.4, allowing only positive ISWs, whereas at deeper the isobath 1750 m only negative ISWs are expected.

The spatial variability of the coefficients α and α_1 has strong implications for the dynamics of internal waves. It was found that ISWs generated at the shelf break in the area of the mooring ST1 are the waves of depression (Vlasenko et al., 2014). However, the weakly nonlinear theory predicts that after passing the turning point at H=850 m these waves have to change their polarity or transform into a breather. Probably the proximity of mooring

6

ST1 to the turning point is the reason why the vertical structure of ISWs shown in Fig.3 a does not fit the structure of the first baroclinic mode. To learn more about the wave dynamics in the area and to check whether a dramatic transformation of ISWs propagated seaward as predicted by the weakly nonlinear theory is correct, a series of numerical experiments on the antishoaling of ISWs was conducted. We restrict our interests to a 2D-version of the problem in order to have a fine resolution grid that allows a more accurate reproduction of the cross-slope wave transformation.

2.2. Numerical modelling

In numerical experiments with seaward propagating ISWs the vertical and horizontal grid steps were Δz=10 m and Δx=7.5 m, respectively, and the buoyancy frequency was set as that shown in Fig.2 a by the thin line. The bottom profile was defined along the cross-section depicted in Fig.1. Initial fields for this series of model runs were prepared as it was done in Vlasenko et al. (2009). An 80 m amplitude first-mode K-dV ISW of depression propagating in a basin of 200 m depth was used for the model initialization. Being inserted into the numerical scheme it started to evolve due to strong nonlinearity into a new solitary wave. This new-born stationary 53 m amplitude "numerical" ISW was used afterwards as an initial condition in the experiments on antishoaling.

Seaward propagation of ISW is presented in Fig.5. Here the horizontal and vertical velocity fields overlaid with the temperature field at different stages of the wave evolution are shown in the middle and bottom panels, respectively. In order to have a guess whether the propagated ISW can be visible on syntetic aperture radars (SAR) images, the top panel represents

7

the wave-induced horizontal velocity gradient du/dx at free surface $z = 0$. According to Alpers (1985) the radar recognises ISWs as systems of bright and dark bands if the wave signal $du/dx(z = 0)$ is of the order of $10^{-3}\,\mathrm{s}^{-1}$.

Analysis of Fig.5 shows that in the shelf break area where the water depth is less than $850\,\mathrm{m}$, the ISW behaves as the weakly nonlinear theory predicts, i.e. in the course of evolution a negative ISW adjusts its structure adiabatically to the varying topography. After passing the turning point where the quadratic nonlinearity changes its sign (see Fig.4), the ISW starts to transform, but not exactly as the weakly nonlinear theory predicts. Instead of changing its polarity in the whole water column the wave turns into a second-mode ISW. As a confirmation of that, in the deep part of the basin where the depth exceeds $1100\,\mathrm{m}$ the horizontal velocity changes its sign twice from the surface to the bottom revealing properties of the second mode (the most right panel in Fig.5 b). This conclusion is also confirmed by the counterphase displacements of the isotherms in the surface and bottom layers, and by the spatial structure of the vertical velocity shown in Fig.5 c.

The process of energy conversion from lower to higher modes continues to progress in the course of the wave evolution. Being a second-mode wave at the $1700\,\mathrm{m}$ isobath (its structure is shown in two left panels in Fig.6), the seaward propagated ISW transforms into a packet of third-mode internal waves at a depth of $4000\,\mathrm{m}$ (two right panels in Fig.6). Thus, it is clear from the comparison of the weakly-nonlinear theory predictions and the fully-nonlinear model output that the theory correctly predicts the positions of the turning points, but fails to describe disintegration of ISWs into packets of higher modes.

One of the possible reasons for such unexpected transformation of the propagated ISWs could be inapplicability of the weakly non-linear theory over the continental slope. In fact, the Gardner equation (2) is valid for shallow water systems when $\lambda/H \gg 1$ (λ is the wave length and H is water depth). The horizontal scale of the initial $53\,\mathrm{m}$ ISW on the 200 m depth shelf is about $1.5\,\mathrm{km}$ (i.e. $\lambda \approx 750\,\mathrm{m}$), so formally this ISW can be classified as a long wave. However, over the continental slope and in the open part of the sea this condition is not valid. To check whether the ratio of the wavelength to the water depth is a key parameter controlling the wave evolution (and applicability of the shallow water theory), another experiment with a $2\,\mathrm{m}$ amplitude (and three times longer wavelength) ISW was conducted. However, it was found that, similar to the large amplitude ISWs, the $2\,\mathrm{m}$ amplitude ISW also reveals strong energy transfer from the first to highest modes in the course of its evolution (not shown here). In fact, the sensitivity runs have confirmed that the energy transfer to the higher modes over an inclined bottom does not depend on the amplitude/wavelength ratio.

Another reason for the cross-mode energy transport could be the steepness of the bottom topography. It is equal to 0.13 (or 7.5°) between the 600 and $1000\,\mathrm{m}$ isobaths. In situations when the wave crosses strong horizontal gradients, the transfer of wave energy to higher modes is quite possible. In order to check whether this is the case, some extra numerical experiments were conducted. In a new series of model runs all settings were the same as above except for the bottom steepness which was reduced to 0.01 (i.e. 0.6°).

Three fragments of the wave antishoaling over the flat topography are shown in Fig.7. The spatial structure of the horizontal velocity reveals the

9

properties of the first mode at all stages of wave evolution. There is still evidence of the energy leak to the second and third modes in the wave tail (find the wave fragment between 55 and 70 km), but this fragment accounts for only 3% of the total energy of the initial ISW.

Thus, this experiment has confirmed that steep topography is the main reason for the energy transfer from the first mode ISW to the higher modes. Presumably, evidence of such a transformation was recorded at the deep mooring ST1, Fig.3 d. Note also that collapse of the seaward propagated ISW over steep topography was accompanied by a radiation of several wave systems overtaking the main wave packet. The process of wave radiation is clearly seen in the Hovmöller diagram presented in Fig.8 a. Here the instant profiles of the free surface velocity are shown for 45 hours of wave evolution.

Fig.8 a shows that an internal wave train is radiated forward after the ISW passes the 850 m isobath. In the Hovmöller diagram this wave system is marked by the arrow with number 1. In the deep part of the ocean this packet has amplitude less than 10 m, and propagates here with velocity $2.38 \, \mathrm{m\,s^{-1}}$, which is close to the value $2.45 \, \mathrm{m\,s^{-1}}$ predicted by BVP (1) for the first baroclinic mode (the blue line in Fig.8 b). Vertically the structure of this leading wave system (not shown here) resembles first baroclinic mode.

A few hours later when the wave system passes the 1800 m isobath a second wave packet detaches from the main wave train and overtakes it (find arrow 2 in Fig.8 a,). An average propagation speed of the new born packet is equal to $1.08 \, \mathrm{m\,s^{-1}}$, which almost ideally coincides with the second eigenvalue of the BVP (1), $1.10 \, \mathrm{m\,s^{-1}}$.

It is interesting that the phase speed of the strongest wave fragment over

10

210 the slope (find arrow 4 in Fig.8 a) remains constant, viz. $0.42\,\mathrm{m\,s^{-1}}$, during

211 four days of evolution. At the beginning of the ISW antishoaling this velocity

212 was equal to the phase speed of the first baroclinic mode on the shelf (dotted

213 line in Fig.8 b). At the latest stages of ISW evolution, i.e. in the deep water

214 part of the basin, this value is close to the phase speed of the fourth baroclinic

215 mode. Evidence of higher baroclinic modes can be seen in vertical structure

216 of the horizontal and vertical velocity fields shown Figs.6 e and 6 f.

3. T-beam generation of ISWs in the far field

218 It was shown above that the ISWs generated over the shelf break and

219 propagated seaward disintegrate into packets of the first, second, and higher

220 baroclinic modes losing a large proportion of their initial energy. As a result,

221 the surface signal $du/dx(z = 0)$ of propagated $53\,\mathrm{m}$ amplitude ISW drops

222 from initial $1.5{\cdot}10^{-3}\,\mathrm{s^{-1}}$ on the shelf to $0.03{\cdot}10^{-3}\,\mathrm{s^{-1}}$ in the deep part (see

223 Figs.5 a and 6 d). Therefore, it is unlikely that propagated seaward ISWs can

224 be observed far from the shelf break. Note, however, that the remote sensing

225 data presented by New and Da Silva (2002) for the Bay of Biscay (BB)

226 (45-48°N, 5-9°W, Fig.1), clearly show evidence of ISWs at a distance of 120-

227 150 km (hereafter the "far field"), see Fig.1 b. Scrutiny of the ISW signature

228 pattern also shows that there is no strong evidence of ISWs between the shelf

229 break area (hereafter "near field") and the far field. Only a few wave systems

230 are presented there.

231 New and Pingree (1990, 1992) and Pingree and New (1989, 1991) ex-

232 plained the appearance of internal waves in the far field in terms of local

233 generation. In short, this mechanism suggests that the tidal internal waves

11

generated over a supercritical topography are radiated from the shelf break to the abyss in the form of a tidal beam (hereafter "T-beam") along one of the characteristics lines

$$\int \frac{dz}{\gamma(z)} = \pm x + \text{const}, \quad \gamma(z) = \sqrt{(\sigma^2 - f^2)/(N^2(z) - \sigma^2)}, \qquad (5)$$

of the hyperbolic wave equation:

$$w_{xx} - \gamma^2(z)w_{zz} = 0. \qquad (6)$$

Here w is the vertical velocity, σ is the M$_2$ tidal frequency, f is the Coriolis parameter. After reflection from the bottom the T-beam returns to the surface 120 km away from the shelf break where it hits the pycnocline and generates internal waves. Gerkema (2001) confirmed the possibility of this mechanism for the BB theoretically using simplified stratification with mixed surface layer and two underlying layers with constant stratification. Schematically, the idea of the T-beam generation is presented in Fig.1 c.

Note that considered here area is next to the BB, Fig.1. As such two basins should have similar conditions for internal wave generation, viz. fluid stratification, bottom profiles, and tidal forcing. If so, a similar appearance of ISWs in the far field of two basins is expected. To investigate the local generation of ISWs by a T-beam in the far field a two-dimensional version of the fully nonlinear nonhydrostatic MITgcm was applied.

The model domain was chosen to be long enough to reproduce the internal waves in the far field. The bottom profile was similar to those used in the experiments with ISW antishoaling, Fig.1. The spatial resolution was Δx=15 m and Δz=10 m. The tidal forcing was defined using the ADCP measurements for the period of 25-27 June 2012 (days 177-179 of 2012) when

12

the strongest ISWs were recorded at mooring ST1, Fig.3. The amplitude of tidal discharge in northern and eastern directions was equal to $60\,\mathrm{m^2\,s^{-1}}$. The background vertical viscosity and diffusivity coefficients were taken at a minimum level, i.e. $10^{-5}\,\mathrm{m^2 s^{-1}}$, but with the Richardson number parametrization for extra mixing in the areas with hydrodynamic instabilities produced by internal waves. The coefficients of horizontal viscosity and diffusivity were set constant, $0.1\,\mathrm{m^2 s^{-1}}$.

Two buoyancy frequency profiles, (i) a smoothed climatic one based on the Boyer et al. (2009) data set, and (ii) an instant profile taken from the D376 yo-yo CTD cast to $1200\,\mathrm{m}$ depth extended by the climatic data below $1200\,\mathrm{m}$, were used in modelling. These two profiles are shown in Fig.2 a by the thick and thin lines, respectively. The difference between the model outputs obtained for both cases is discussed below.

3.1. Smoothed stratification

The dynamics of internal waves can be studied using the Hovmöller diagram, Fig.9 a. It shows the evolution of vertical displacement (left axes) of the 13°C isotherm during the time span 240-252 h (right axes) after the beginning of the experiment. Fig.9 b represents the amplitude of the horizontal velocity during the 21-st tidal cycle. A long term spin-up of the model was required to allow higher baroclinic tidal modes to propagate through the whole model domain. Their superposition results in the formation of a tidal beam that is clearly seen in both the near and far fields, Fig.9 b.

The T-beam is quite a narrow band with a high intensity of baroclinic tidal energy. It starts at point (a) on the shelf edge and propagates downward to the abyss along the characteristic line (5) that is depicted in Fig.9 b by

13

the dashed white contours. After reflection from the bottom at point (b) the baroclinic tidal energy returns back to the surface at point (c).

In the shelf break area (between 10 and 20 km) Fig.9 a shows evolution of two systems of short waves generated over the shelf break. The first group comprises two wave packets (1)-(2)-(3) highlighted by yellow colour. It seems that both packets, one directed to the shelf and another to the open sea, were generated according to the lee wave mechanism. The other wave system shown in orange (fragments (4)-(7)) was developed due to steepening and disintegration of propagating internal tidal wave (Vlasenko et al., 2005). Both systems remain visible during one additional tidal cycle and attenuated in the deep part of the sea according to the mechanism of disintegration discussed in Section 2.

On the other side of the model domain, i.e. in the far field, the wave motions are also well developed. The strongest wave system (8)-(9) (in Fig.9 a it is marked by blue colour) starts to develop at point (c) where the tidal beam hits the pycnocline located just below the free surface (at $50\,\mathrm{m}$ depth, see Fig.2 a). At the first stage the generated wave looks like a bore propagated seaward. It becomes steeper in the course of nonlinear evolution gradually transforming into a packet of rank-ordered ISWs.

The propagation speed of the wave fragment (8)-(9) calculated on the basis of the Hovmöller diagram, Fig.9 a, is equal to $0.61\,\mathrm{m\,s^{-1}}$, which is well below the phase speed of the first mode ISWs, but close to the velocity of the third mode (first four eigenvalues of the BVP (1) for the depth $4.3\,\mathrm{km}$ are equal to 2.52, 1.23, 0.68, and $0.45\,\mathrm{m s^{-1}}$, respectively). Thus, the slow velocity of propagation suggests that specific features of the high baroclinic

14

modes should be evident in the vertical stucture of the wave packet (8)-(9).

Fig.10 represents the displacements of isotherms and the vertical velocity of the wave packet depicted in right bottom corner of Fig.9 a by a magenta rectangle. It is clear from Fig.10 a that the leading wave in this packet is the wave of depression in the surface 200 m layer (maximum displacements up to 35 m), but it is the wave of elevation between 800 m and 1100 m depths. The high mode wave structure is more evident in Fig.10 b which shows that the vertical velocity changes its sign twice along the dashed line in panel Fig.9 b, which is a specific feature of the third mode.

One can also identify in Fig.9 b a secondary tidal beam originated at point (d) located in the layer of the main pycnocline, i.e. around 900 m depth, see Fig.2 a. This beam propagates to the surface along the characteristic line, where it is reflected from the surface downward at point (e), and ultimately ends up at the bottom at point (f). The explanation of this phenomenon can be found in terms of the mechanism of scattering of the main tidal beam from layers with a sharp change of vertical stratification discussed below.

3.2. D376 buoyancy frequency profile

The buoyancy frequency profile recorded during cruise D376 was used in the next series of numerical experiments. As seen from Fig.2 a, the instant profile (shown by the thin line) is highly corrugated in the layer of the main pycnocline, specifically between 750 m and 1200 m depths. High intermittency of vertical fluid stratification creates favourable conditions for internal wave reflection from layered fluid structures. The effect of tidal beam reflection from a pycnocline was reproduced numerically by Gerkema (2002) and proven in laboratory experiments by Wunsch and Brandt (2012). There

15

are only a few specific profiles of the buoyancy frequency (see (Magaard, 1962; Vlasenko, 1987)) that allow internal wave propagation without reflection. Sharp increase or decrease of the vertical density gradients can lead to a massive reflection of the tidal beam energy (Grimshaw et al., 2010)

The T-beam energy reflection from the layers with sharp changes of buoyancy frequency is illustrated in Fig.11. The intermittent layered structure of the main pycnocline between 750 m and 1200 m depths resulted in a stronger secondary tidal beam (d)-(e), Fig.11 b, than it was for the smoothed profile, Fig.9 b. Moreover, an additional tidal beam, viz. (g)-(h), has appeared in Fig.11 b. It was generated by reflection of the tidal energy of the main beam (a)-(b) from a number of layers of intermittent stratification in the main pycnocline. As a consequence of this strong internal energy reflection, the main tidal beam (a)-(b) below 1500 m is much weaker in Fig.11 b than it was in Fig.9 b. In other words, a large part of the beam energy returns to the surface in the area between the far- and near fields. In this area the secondary tidal beams (d)-(e) and (g)-(h) interact with the subsurface pycnocline and generate locally two new wave systems depicted in Fig.11 a by numbers (1)-(2) and (3)-(4).

The intensity of the signals produced by wave systems (1)-(2) and (3)-(4) at the free surface is strong enough to be visible from space by SARs. The derivative $du/dx(z = 0)$ of the model output at $t =$252 h is shown in Fig.12 a. Note, however, that the spatial and temporal characteristics of these wave two systems are quite different. The speed of propagation of the wave packet (1)-(2) is equal to $0.61 \, \mathrm{m \, s^{-1}}$, which coincides with the phase speed of the ISW packets (6)-(7) and (8)-(9) shown in Fig.9 a. Moreover, spatially

16

all these wave packets are mostly rank-ordered (see, for instance, Fig.12 b) resembling a third baroclinic mode in the vertical direction, Fig.12 d.

Wave system (3)-(4) is quite different from packet (1)-(2). It propagates much slower, i.e. with average speed $0.17\,\mathrm{m\,s^{-1}}$ (see Fig.11 a). Further analysis of its spatial structure has shown that the wave system (3)-(4) can be classified as an internal wave breather (Lamb et al., 2007), i.e. a localised wave packet with a sinusoidal periodic carrier that is restricted in space by a soliton-shape envelope, as shown Fig.12 c. Weakly nonlinear theory predicts such quasi-stationary solutions, internal breathers, that remain stable in the course of their propagation. Fig.11 a shows that wave packet (3)-(4) does keep its form at least one and a half tidal period until it was overtaken by another wave group.

In fact, the phase speed of the carrier wave should not necessarily coincide with the propagation velocity of the breather, i.e. the group speed. For the surface wave in deep water, for instance, the phase speed of the breather's carrier is double as high as the group speed (Zakharov, 1968; Slunyaev and Shrira, 2013). In the present case the phase speed of the carrier is equal to $0.30\,\mathrm{m\,s^{-1}}$, which is almost twice as high as the breather's speed. This value was calculated using the frequency of the carrier wave 0.0025 s^{-1} (found from the model by sampling at several fixed points that the breather crosses) and an average wavelength $660\,\mathrm{m}$ of the wave carrier detected from Fig.11 (see also Fig.12).

It is interesting to validate the model-predicted parameters of the breather against some theoretical values obtained from the boundary value problem:

$$\frac{d^2\Phi_j}{dz^2} + \frac{k_j^2}{\gamma^2(z)}\Phi_j = 0, \quad \Phi_j(0) = \Phi_j(-H) = 0. \tag{7}$$

17

Here $\Phi_j(z)$ is the vertical structure function and k_j is the wave number of the j-th mode. As distinct from (1), BVP (7) calculates wave numbers and vertical structure of periodic internal waves. The dispersion relations of the first three baroclinic modes are shown in Fig.13. For the wave carrier with frequency 0.0025 s^{-1} and the fluid stratification shown in Fig.2 a the wave length, phase speed, and the group speed of the first three modes (j=1,2,3) are shown in the Table. The model-predicted parameters of the numerical breather carrier from the Hovmöller diagram, Fig.11 a, are as follows: the wavelength - 600 m, phase speed - 0.30 m s^{-1}, and group velocity 0.17 m s^{-1}. It is clear from the Table that the third baroclinic mode provides the best fit to the model predicted parameters of the numerical breather carrier wave. This is also consistent with Fig.12 e, that shows the vertical structure of the breather.

New and Da Silva (2002) analysed parameters of more that 100 ISWs observed in SAR images of the BB (see Fig.1 b), which is next to the considered here area. This data set can be taken as indirect validation of the model output. It was found that the wavelengths of the whole ensemble of observed ISWs ranged from 0.6 to 3.0 km, with a mean value of 1.35 km. The wavelengths $\lambda_1, \lambda_2, \lambda_3$ shown in Fig.12 b are 1.35, 1.15, and 0.85 km, respectively, that is in agreement with the observations by New and Da Silva (2002). It is also interesting that 10% of all reported ISWs were quite short. They had their wavelengths in the range between 600 and 800 m which is consistent with the wavelength λ_4=λ_5=660 m of the internal breather shown in Fig.12 c.

4. Discussion and conclusions

The present study was motivated by the fact that majority of ISWs recorded at the mooring deployed on the continental slope of the Celtic Sea in July 2012 exhibited properties of the second baroclinic mode. In light of the most recent modelling efforts by Vlasenko et al. (2014) who reproduced numerically the three-dimensional dynamics of the baroclinic tides in the area and showed that first-mode ISWs are generated over the shelf break, this observational evidence of higher baroclinic modes over the continental slope required further scrutiny.

A preliminary analysis of the wave dynamics in terms of a weakly nonlinear theory has shown that all ISWs generated over the shelf break and propagated seaward over an inclined bottom must change their form after passing the turning points, i.e. the isobath where the coefficients of the quadratic and cubic nonlinearities of the Gardner equation (2) change their sign. This non-adiabatic behaviour of ISWs was reproduced numerically using the fully nonlinear nonhydrostatic MITgcm. The numerical runs convincingly showed that steepness of the bottom topography is the major factor controlling the process of wave disintegration. It was found, however, that the seaward propagated ISWs do not evolve exactly as the weakly non-linear theory predicts. Quite opposite, after passing the turning point where the coefficient of the quadratic nonlinearity $\alpha=0$, the ISW did not change its polarity but started to transfer its energy to higher modes. This process was accompanied by forward radiation of low-mode internal wave systems. The first-mode wave packet is radiated first, then the second mode, etc, as shown in Fig.8.

It was found that the reason for the energy transfer to higher modes is the

19

steep gradient of the continental slope. Sensitivity runs with much smaller bottom inclinations have shown that ISW really reverses its polarity after passing the turning point according to a classical mechanism predicted by the weakly nonlinear theory.

Overall, the seaward propagated ISWs do not escape far from the shelf break and cannot be observed on SAR images far away from the shelf break. Figs.6 a and 6 d clearly show that in the open part of the sea the surface signal produced by seaward propagated ISWs is much weaker than $10\,\text{s}^{-3}$ which is considered as a threshold for detection of ISWs by SARs (Alpers, 1985). Note, however that these high-mode waves, being invisible from space, are still able to form strong circulation cells at the depths of 1000-1500 m (see Figs.6 b-c and 6 e-f). Ultimate disintegration and wave breaking can lead to strong local water mixing and formation of the intermittent layered stratification of the main pycnocline shown in Figs.2 b-e (Boyer et al., 2009).

The appearance of internal waves in the far field is explained here in terms of the spatial structure of baroclinic tides. A tidal beam is generated over supercritical topography and propagates downward from the shelf break to the abyss along the characteristic line $\int 1/\gamma(z)dz = x + \text{const}$ of the hyperbolic wave equation (5). After reflection from the bottom the tidal beam returns to the free surface in the far field where it hits the pycnocline and generates internal waves.

The MITgcm reproduced the tidal beam over the shelf break of the Celtic Sea quite accurately. The model predicted wave velocities inside the tidal beam (up to $16\,\text{cm}\,\text{s}^{-1}$ during the spring tide) and its spatial position were consistent with that recorded at the deep water mooring deployed in the BB

58 km from the shelf break (Pingree and New, 1991). The new element found in the present study concerns the vertical structure of the ISWs in the far field. The model reproduced third-mode ISW packets generated locally. An example of such a wave packet is shown in Fig.12.

It should be noted here that Grisouard and Staquet (2010) in their numerical analysis of the T-beam generation of internal waves in the BB also reproduced the second mode in the far field (their Figs.2 and 3). It is interesting that in the earliest publications by New and Pingree (1990, 1992), and in a more recent interpretational paper by New and Pingree (2000) the observed in the BB ISWs were treated as the first-mode waves. Unfortunately, it is not possible to confirm or disprove this fact from the provided observational data that cover only a surface 150 m layer. The temperature time series presented in Fig.3 a also shows all ISWs as waves of depression near the surface, but they clearly reveal properties of higher modes in the deep, Fig.3 d.

An indirect confirmation of the modal structure of ISWs can be deduced from their phase speed calculated based on SAR images. New and Da Silva (2002) analysed satellite images assuming the first-mode phase speed of the observed waves which is close to $1\,\mathrm{m\,s^{-1}}$. However, Envisat-ASAR image from the middle of the BB dated 12 August 2005 and published in (Muacho et al., 2014) (their Figure 2) allows one to calculate this value very accurately. The image presented in Fig.14 clearly shows at least nine circular wave fronts with an average distance between them of about 25 km. Assuming a semidiurnal tidal periodicity of the observed waves it can be found that their phase speed must be equal to $0.55\,\mathrm{m\,s^{-1}}$, which is close to $0.6\,\mathrm{m\,s^{-1}}$, i.e. the model

21

predicted phase speed found from Fig.11. It is interesting that Grisouard and Staquet (2010) in their numerical experiment E2 also found that the two wave trains were separated by 25-30 km, meaning that these ISWs propagate at almost half of the speed estimated by New and Pingree (1990); New and Da Silva (2002).

A series of sensitivity runs with smoothed and realistically intermittent fluid stratification has shown that sharp changes of the vertical fluid stratification are the sites of internal wave reflection. As a result of strong internal wave reflection from a layered main pycnocline quite a substantial part of the T-beam energy propagated from the shelf break downward to the abyss returns to the surface in the area between the near- and the far fields where it generates locally some extra internal wave systems. Numerical evidence of this effect is shown in Fig.11. This could be a reasonable explanation of why ISW packets are still visible in SAR images between the near- and far fields.

Note also that the backward reflection of the T-beam from the layers with intermittent stratification was conducted here for a relatively smoothed stratification (see Fig.2 a) that was found by averaging of 14 instant buoyancy frequency profiles recorded in D376 cruise at the yo-yo CTD station. The effect of T-beam reflection can be even stronger in case of real instant profiles that are much more "fuzzy", Figs.2 b-e. Four of them acquired from Boyer et al. (2009) are shown in Fig.2 b-e. They reveal very strong local layering between 500 m and 2000 m depths that can provide much stronger T-beam reflection.

Another finding from the present study is shown in Figs.12 c and e. Analysis of all characteristics of this wave system generated by the secondary tidal

22

beam, Fig.11, has shown that this wave packet can be classified as an internal wave breather. First of all, it is not rank-ordered; maximal amplitudes are located in the middle of the packet. It was found that this wave system propagates as a periodic wave train with a soliton envelope. Most importantly, this form is stable in space and time (see Fig.11, wave (3)-(4)). Secondly, this packet propagates much slower than the rank-ordered wave packets. Moreover, the group speed of this packet is twice as small as the phase speed of the carrier wave. Theory-wise, all these characteristics are associated with internal wave breathers that are probably generated in the far field, but some further research is required.

23

References

Alpers, W. (1985) Theory of radar imaging of internal waves. *Nature*, 314, 245-247.

Baines, P.G. (1982) On internal tide generation models. *Deep Sea Res. I, 29 (3A)*, 307-339.

Boyer, T. P., J. I. Antonov, O. K. Baranova, H. E. Garcia, D. R. Johnson, R. A. Locarnini, A. V. Mishonov, T. D. OBrien, D. Seidov, I. V. Smolyar, M. M. Zweng, 2009. World Ocean Database 2009. S. Levitus, Ed., NOAA Atlas NESDIS 66, U.S. Gov. Printing Office, Wash., D.C., 216 pp.

Gerkema, T. (2001) Internal and interfacial tides: beam scattering and local generation of solitary waves. *J. Mar. Res.*m *59*, 227-255.

Gerkema, T. (2002) Application of an internal tide generation model to baroclinic spring-neap cycles. *J. Geophys. Res., 107(C9)*, doi:10.1029/2001JC001177.

Gerkema, T., F. A. Lam, and L.R.M Maas. (2004) Internal tides in the Bay of Biscay: conversion rates and seasonal effects. *Deep-Sea Research II, 51*, 2995-3008.

Grimshaw R., E. Pelinovsky, and T. Talipova (1997) The modified Korteweg - de Vries equation in the theory of large-amplitude internal waves. *Nonlinear Processes in Geophysics, 4*, 237-250.

Grimshaw R., E. Pelinovsky, and T. Talipova (1999) Solitary wave transfor-

24

mation in a medium with sign-variable quadratic nonlinearity and cubic nonlinearity. *Physica D), 132*, 132, 40-62.

Grimshaw, R., E. Pelinovsky, T. Talipova, and A. Kurkin (2004) Simulation of the transformation of internal solitary waves on oceanic shelves. *J. Phys. Oceanogr., 34(12)*, 27742791.

Grimshaw R., E. Pelinovsky, and T. Talipova (2010) Non-reflecting internal wave beam propagation in the deep ocean *J. of Phys Oceanogr., 40*, 802-813.

Grisouard, N. ,and C. Staquet (2010) Numerical simulations of the local generation of internal solitary waves in the Bay of Biscay, *Nonlin. Processes Geophys. , 17*, 575-584, doi:10.5194/npg-17-575-2010.

Holt, J.T., and S.A. Thorpe (1997) The propagation of high frequency internal waves in the Celtic Sea. *Deep Sea Res. I, 44(12)*, 2087-2116.

Hopkins, J., J. Sharples, and J. M. Huthnance (2012) On-shelf transport of slope water lenses within the seasonal pycnocline. *Geoph. Res. Letter, 39*, L08604, doi:10.1029/2012GL051388.

Huthnance, J.M., H. Coelho, C.R. Griffiths, P.J. Knight, A.P. Rees, B. Sinha, A. Vangriesheim, M. White,and P.G. Chatwin (2001) Physical structures, advection and mixing in the region of Goban spur. *Deep Sea Res. II, 48(14-15)*, 2979-3021.

Egbert, G.D., and S.Y. Erofeeva (2002) Efficient inverse modeling of barotropic ocean tides, *J. Atmos. Oceanic Technol., 19(2)*, 183-204.

Inall, M.E., D. Aleynik, T. Boyd, M.R. Palmer, and J. Sharples (2011) Internal tide coherence and decay over wide shelf sea. *Geophys. Res. Let.*, *38*, L23607.

Lamb, K.G., O. Polukhina, T. Talipova, E. Pelinovsky, W. Xiao, and A. Kurkin (2007) Breather generation in fully nonlinear models of stratified fluid. *Phis. Rev.*, *E 75*, 046306.

Magaard, L. (1962) Zur Berechnunginterner Wellen in Meeresraeumen mit nich-ebenen Bodenbei einer speziellen Dichteverleitung *Meeresforsch.*, Kiel, *18*, 161-183.

Marshall, J., A. Adcroft, C. Hill, L. Perelman, and C. Heisey (1997) A finite-volume, incompressible Navier-Stokes model for studies of the ocean on the parallel computers, *J. Geophys. Res.*, 102, 5733-5752.

Muacho, S., J.C.B. da Silva, V. Brotas, P.B. Oliviera, J.M. Magalhaes (2014) Chlorophyll enhancement in the central region of the Bay of Biscay as a result of internal tidal wave interaction. *J. of Mar. Sys.*, *136*, 22-30.

New, A.L. and R.D. Pingree (1990) Large-amplitude internal soliton packets in the central Bay of Biscay. *Deep-Sea Res.*, *37(3)*, 513-524.

New, A.L. and R.D. Pingree (1992) Local generation of internal soliton packets in the central Bay of Biscay. *Deep-Sea Res.*, *39*, 1521-1534.

New, A.L. and R.D. Pingree (2000) An intercomparison of internal solitary waves in the Bay of Biscay and resulting from Korteveg-de Vries-type theory. *Progr. in Oceanogr.*, *45*, 1-38.

26

New, A.L. and J.C.B. Da Silva (2002) Remote-sensing evidence for the local generation of internal soliton packets in the central Bay of Biscay. *Deep-Sea Res.I, 49*, 915-934.

Pingree, R.D., and G.T. Mardell (1981) Slope turbulence, internal waves and phytoplankton growth at the Celtic Sea shelf-break, *Phil. Trans. R. Soc. Lond. A, 302*, 663-682.

Pingree, R.D., and G.T. Mardell (1985) Solitary internal waves in the Celtic Sea. *Prog. Oceanogr., 14*, 431-441.

Pingree, R.D., G.T. Mardell, and A. New (1986) Propagation of internal tides from the upper slopes of the Bay of Biscay. *Nature, 321*, 154-158.

Pingree, R.D., and A. New. (1989) Downward propagation of internal tidal energy in the Bay of Biscay. *Deep Sea Res. I, 36(5)*, 735-758.

Pingree, R.D., and A. New. (1991) Abyssal penetration and bottom reflection of internal tidal energy in the Bay of Biscay. *J. Phys. Ocanogr., 21*, 28-39.

Pingree, R.D., and A. New. (1995) Structure, seasonal development and sunglint spatial coherence of the internal tide on the Celtic and Armorican shelves and in the Bay of Biscay. *Deep Sea Res. I, 42*, 245-284.

Slunyaev A., and V. Shrira (2013) On the highest non-breaking wave in a group: fully nonlinear water wave breathers versus weakly nonlinear theory. *J. Fluid Mech., 735*, 203-248

Stashchuk N., V. Vlasenko, M.Inall, and D. Aleynik (2014) Horizontal disper-

sion in shelf seas: high resolution modelling as an aid to sparse sampling. *Progress in Oceanography*, *128*, 74-87.

Vlasenko, V. (1987) The generation of internal waves in stratified ocean of variable depth. *Izvestiya Akademii Nauk SSSr. Fizika Atmosferi i Okeana*, *23*, 300-308.

Vlasenko, V., J.C. Sanchez Garrido, N. Stashchuk, J Garcia Lafuente (2009) Three-dimensional evolution of large-amplitude internal waves in the Strait of Gibraltar. textitJ. of Phys. Oceanogr, textit39, 2230-2246.

Vlasenko, V., N. Stashchuk, and K. Hutter (2005) Baroclinic tides: Theoretical modeling and observational evidence. *Cambridge University Press*, 351pp.

Vlasenko, V., N. Stashchuk, M. Inall, and M. Palmer (2013) Generation of baroclinic tides over an isolated underwater bank. *J. Geophys. Res.*, *118*, 4395-4408.

Vlasenko, V., N. Stashchuk, M. Inall, and J.Hopkins (2014) Tidal energy conversion in a global hot spot: on the 3D dynamics of baroclinic tides at the Celtic Sea shelf break. *J. Geophys. Res.*, *119*, 119, doi:10.1002/2013JC009708.

Wunsch, S., and A. Brandt (2012) Laboratory experiments on internal wave interactions with a pycnocline. *Exp. Fluids*, *53*, 1663-1679.

Zakharov, V. E. (1968) Stability of periodic waves of finite amplitude on the surface of a deep fluid. *J. of Appl. Mechan. and Techn. Phys.*, *9 (2)*, 190-194. doi:10.1007/BF00913182.

Table 1: Parameters of first three baroclinic modes

Mode	Wavelength (m)	Phase speed ($\mathrm{m\,s^{-1}}$)	Group speed ($\mathrm{m\,s^{-1}}$)
1	2346	0.93	0.27
2	890	0.35	0.21
3	675	0.27	0.13
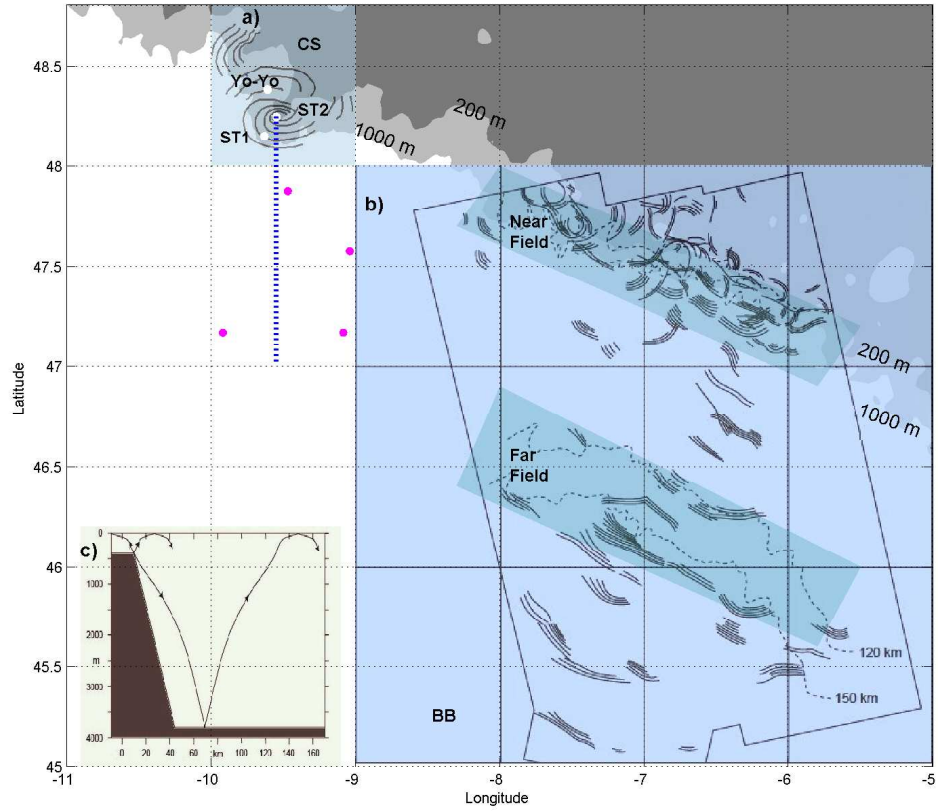
Figure 1: Shelf break of the Celtic Sea presented by the 200 m izobath. Positions of three moorings, Yo-Yo, ST1, and ST2 deployed during cruise D376 are depicted by black dots. Vertical dotted line shows the cross-section used in numerical modelling. a) Plan view of tidally generated internal wave systems predicted by the MITgcm (Vlasenko et al. (2014)). Time interval between two wave fronts equals 2 h. b) Composite image of all ISW packets observed in July 1994 and July-September 1999 in the Bay of Biscay and reported by New and Da Silva (2002). The observational area ranges from 5 to 9°W which is adjacent to the domain considered here. c) The tidal beam that is mentioned in the aforementioned paper as a reason for a local generation of internal waves in the far field.

30
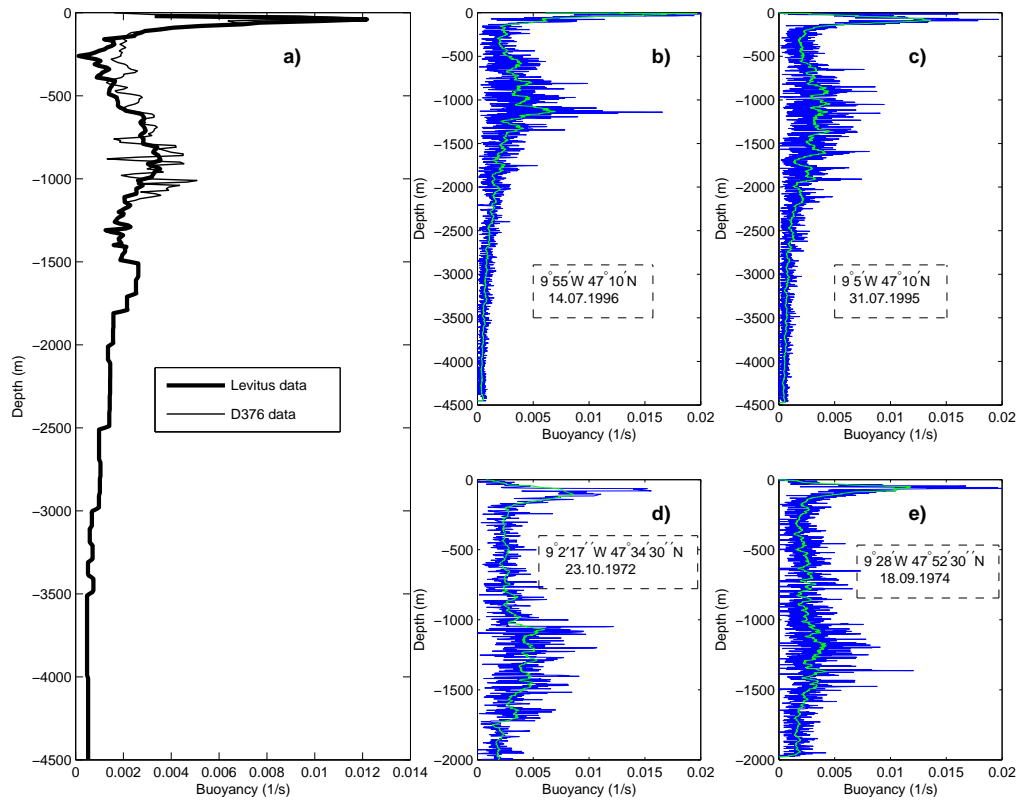
Figure 2: a) Vertical profiles of the buoyancy frequency: recorded at the Yo-Yo station (light line) and produced using the Levitus data set (thick line). Red lines depict the model profiles used in Section 3. b)-e) Buoyancy frequency profiles recorded at four CTD stations shown in Fig.1 by red dotes (Boyer et al., 2009).
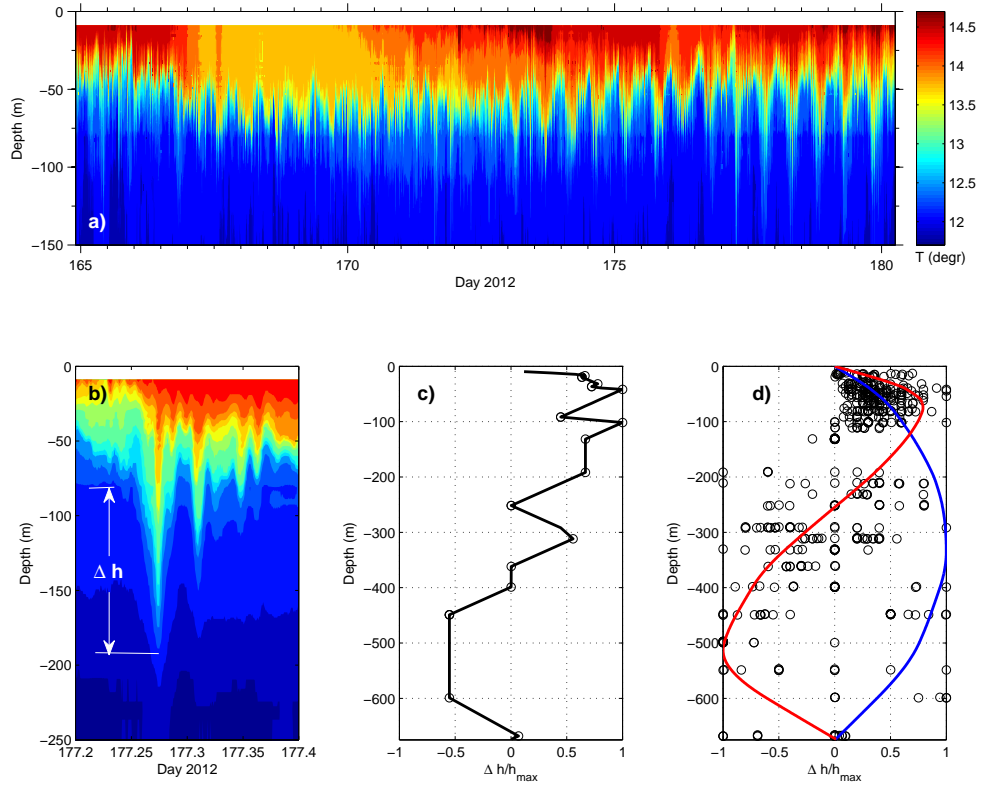
Figure 3: (a,b) Temperature recorded at mooring ST1. (c) Normalized vertical structure function of isotherm displacements of the leading ISW shown in panel (b). (d) The normalised wave displacements of the strongest 45 ISWs recorded at ST1. Blue and red lines show the normalized profiles Φ_1 and Φ_2 of the boundary value problem (1), respectively.
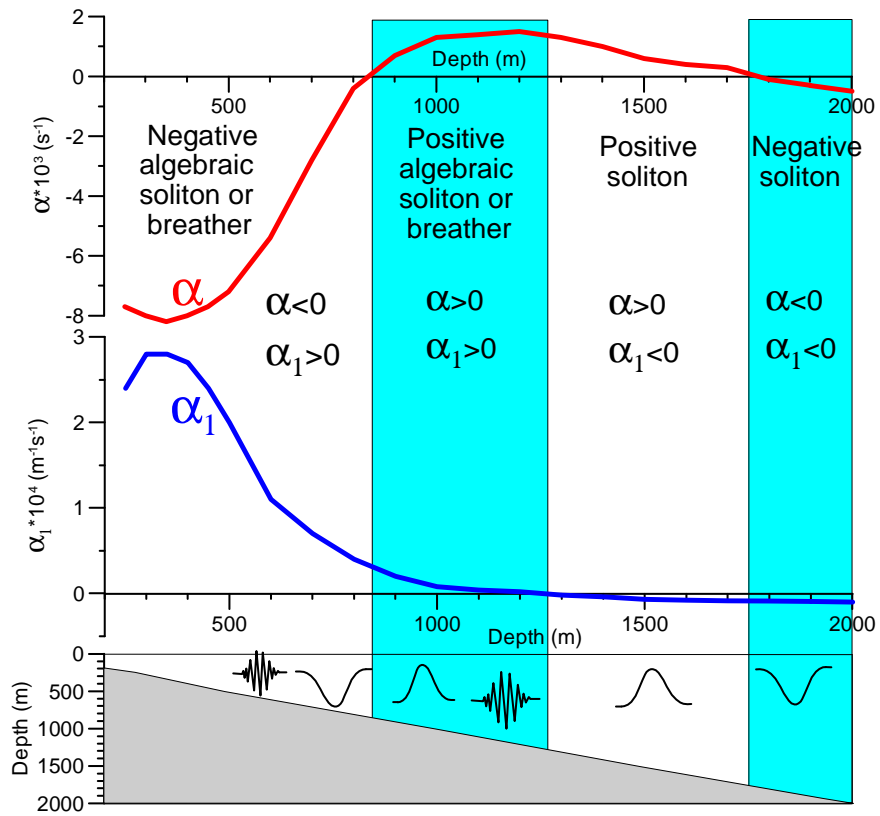
Figure 4: Quadratic α and cubic α_1 coefficients of nonlinearity of the Gardner equation (2) as functions of depth.
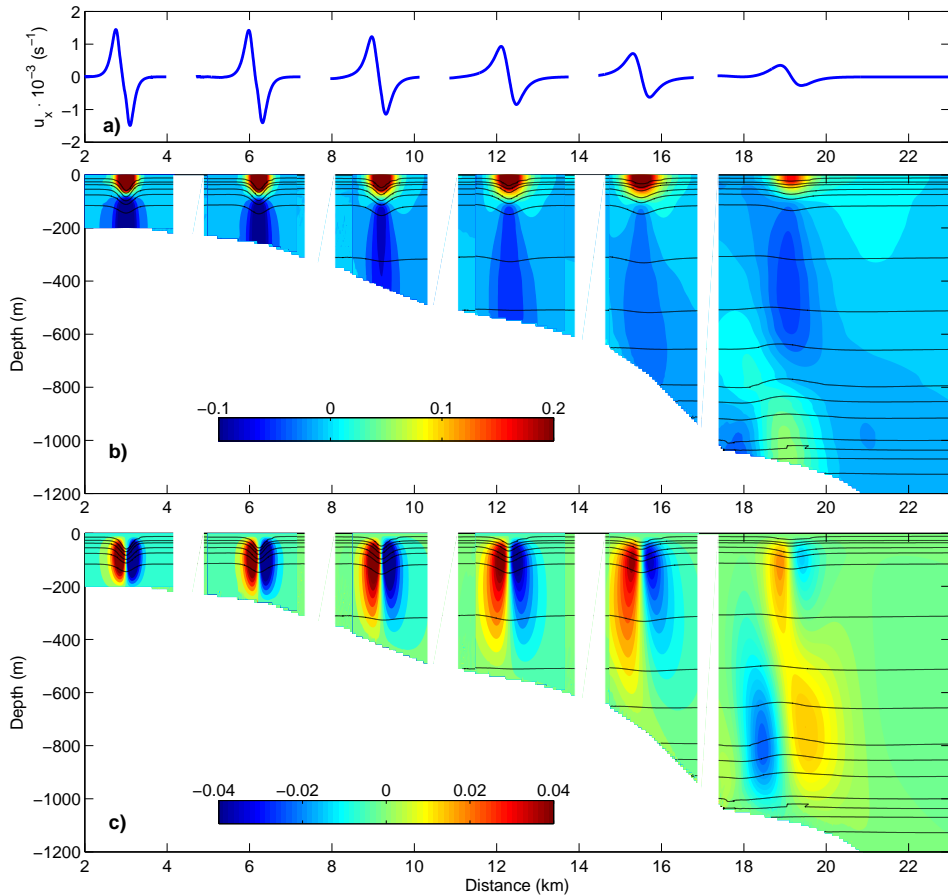
Figure 5: (a) Gradient of the horizontal velocity at the free surface $\partial u/\partial x(z = 0)$, (b) horizontal velocity overlaid with the temperature field and (c) vertical velocity overlaid with the temperature field of the ISW propagated seaward at different stages of its evolution. Colour bars show the velocity in ms^{-1}. Both panels are a composite of six different moments in time. Black solid lines depict isotherms.
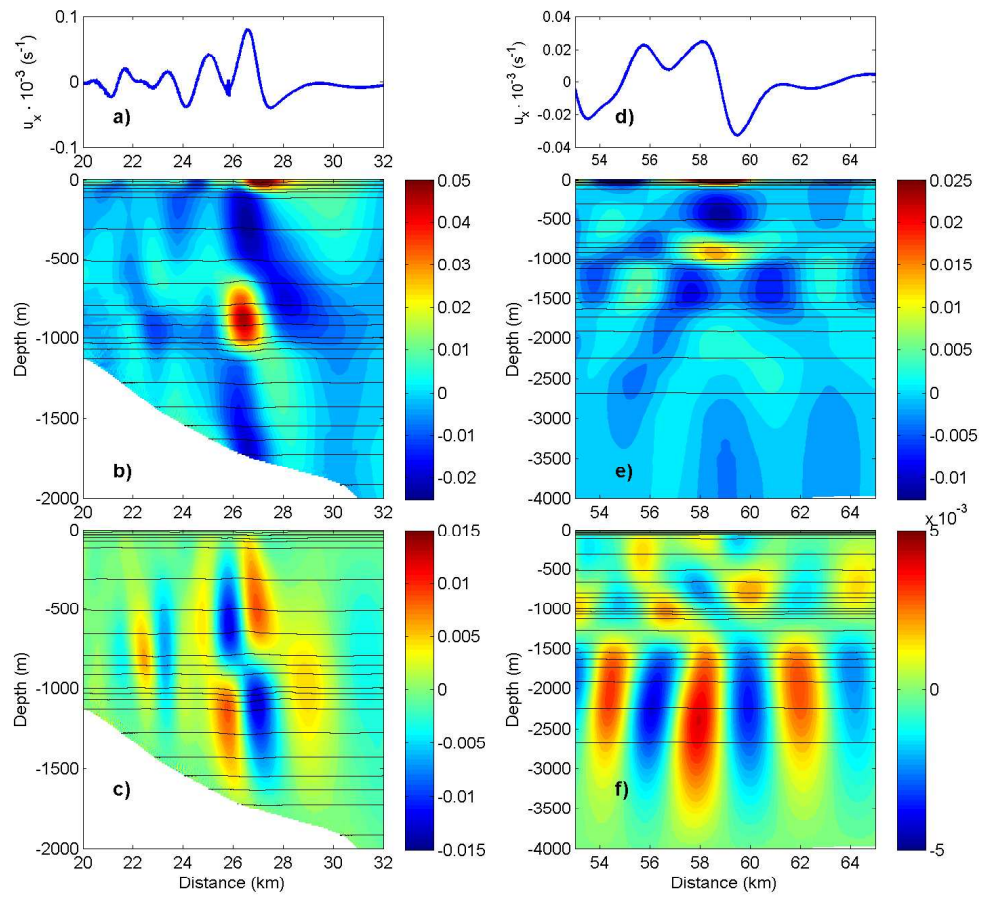
Figure 6: The same as Fig.5 but for the latest stages of ISW evolution.
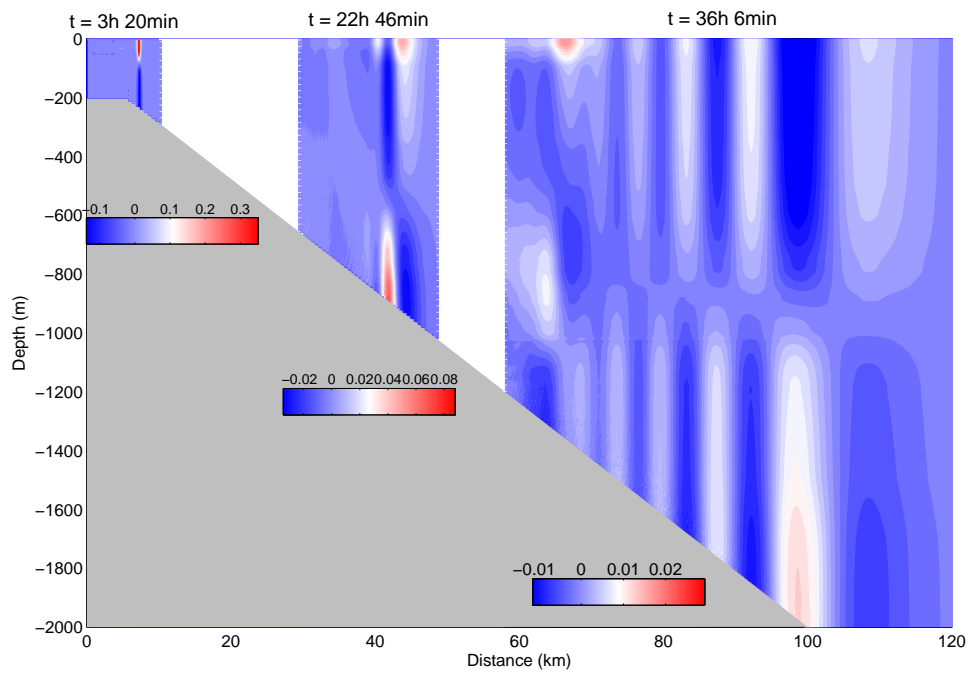
Figure 7: Horizontal velocity of the ISW propagated seaward over a gently sloping topography at three different stages of its evolution.
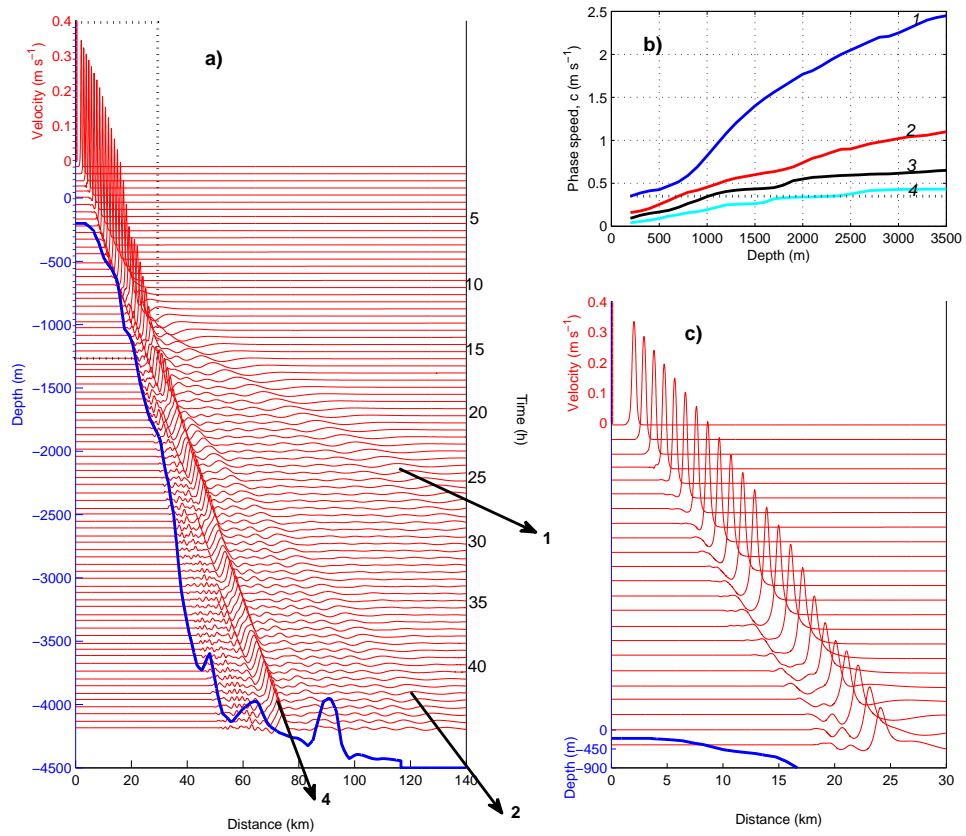
Figure 8: (a) Horizontal velocity produced at the free surface by a 53 m ISW propagated from 200 m deep shelf into the open sea. The time interval between two successive records is 2000 sec. The bottom profile is shown by a blue solid line. Arrows with numbers mark radiated wave packets of the corresponding mode. (b) Phase speed of four first modes calculated using the BVP (1) as a function of depth. (c) Zoom of the fragment depicted in panel (a) by a dashed rectangle.
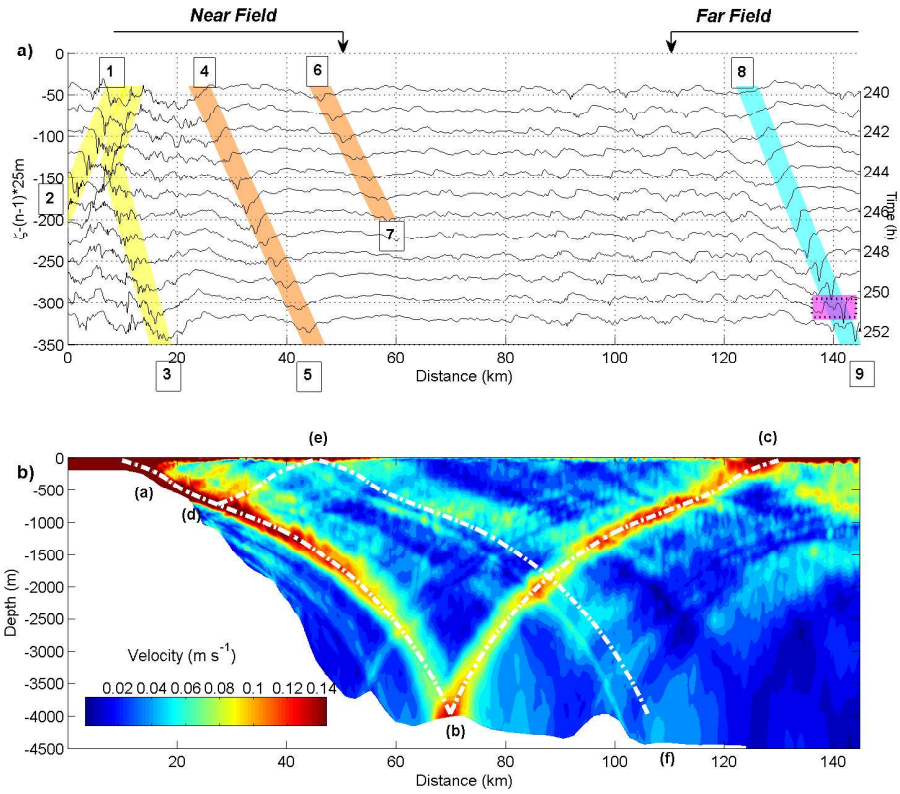
Figure 9: (a) Horizontal profiles of the isotherm 13°C taken with a 1 hour time interval after 20 tidal periods of model time. Vertical displacement ζ of the isotherm from its equilibrium depth of 47 m is calculated using the formula depicted on the vertical axis. Numbers $n =1, 2, ..., 12$ are counted from the topmost curve. (b) Amplitude of horizontal velocity calculated for the time span 240-252 h. The Levitus based buoyancy frequency profile (see Fig.2 a) was used in this run.
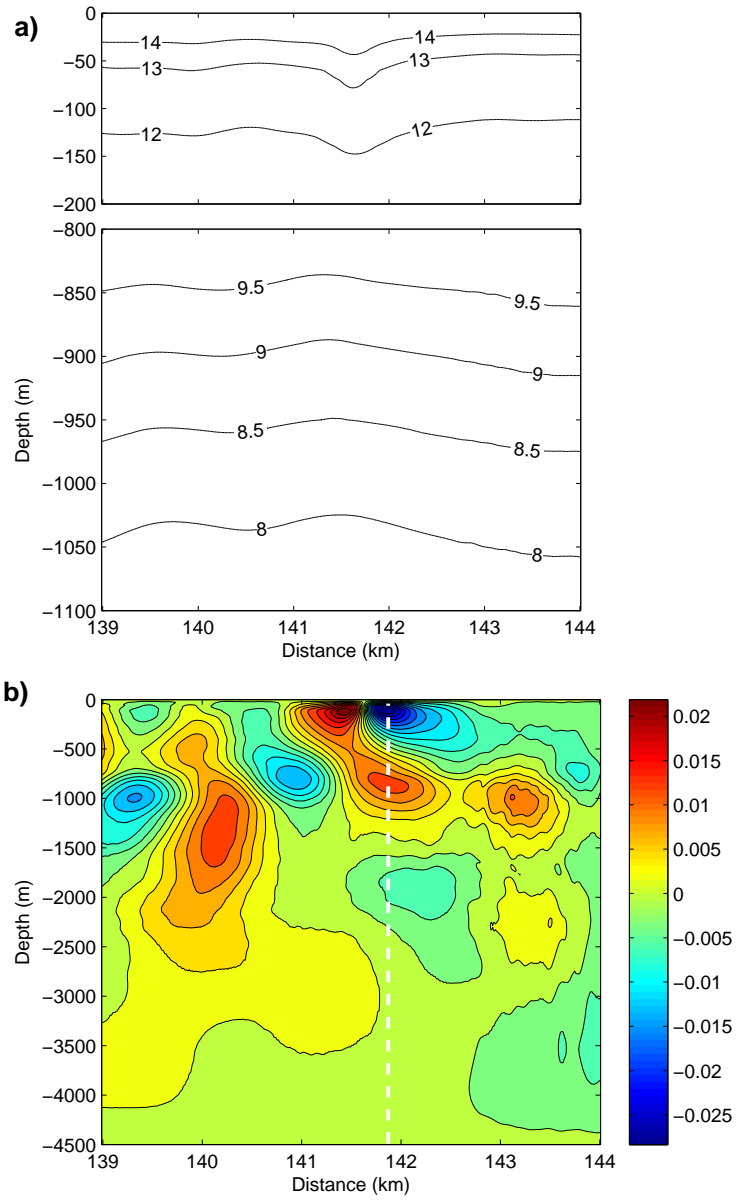
Figure 10: (a) Isotherms and (b) and vertical velocity field of the fragment depicted in Fig.9 a by a magenta rectangle.
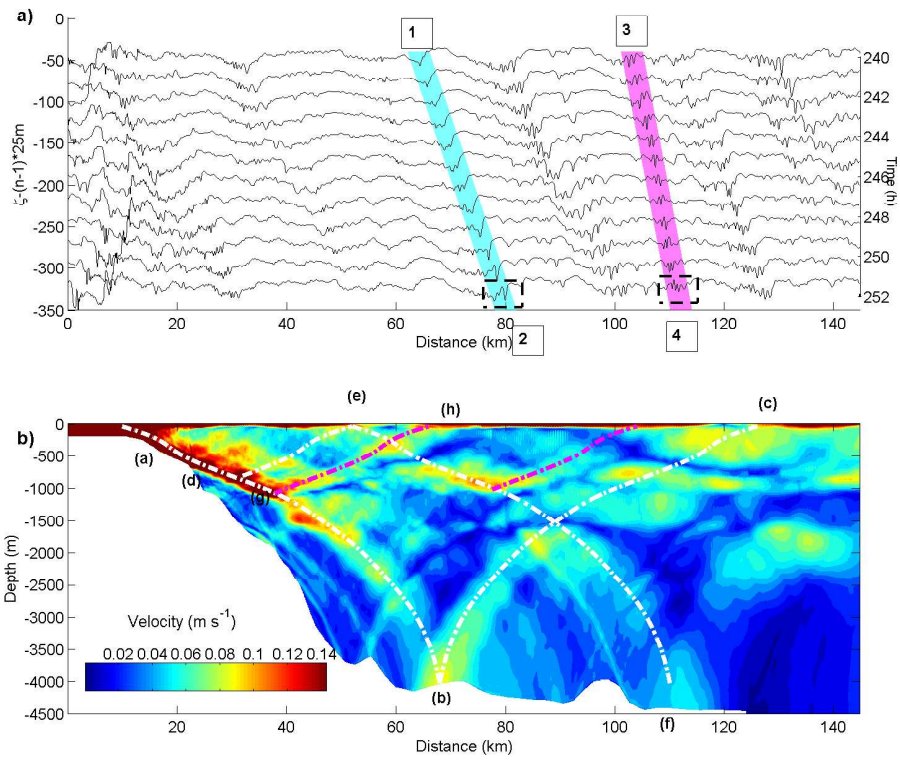
Figure 11: The same as in Fig.9 but for the original buoyancy frequency profile (the thin line in Fig.2 a). Two extra wave systems, (1)-(2) and (3)-(4), are not visible in Fig.9.
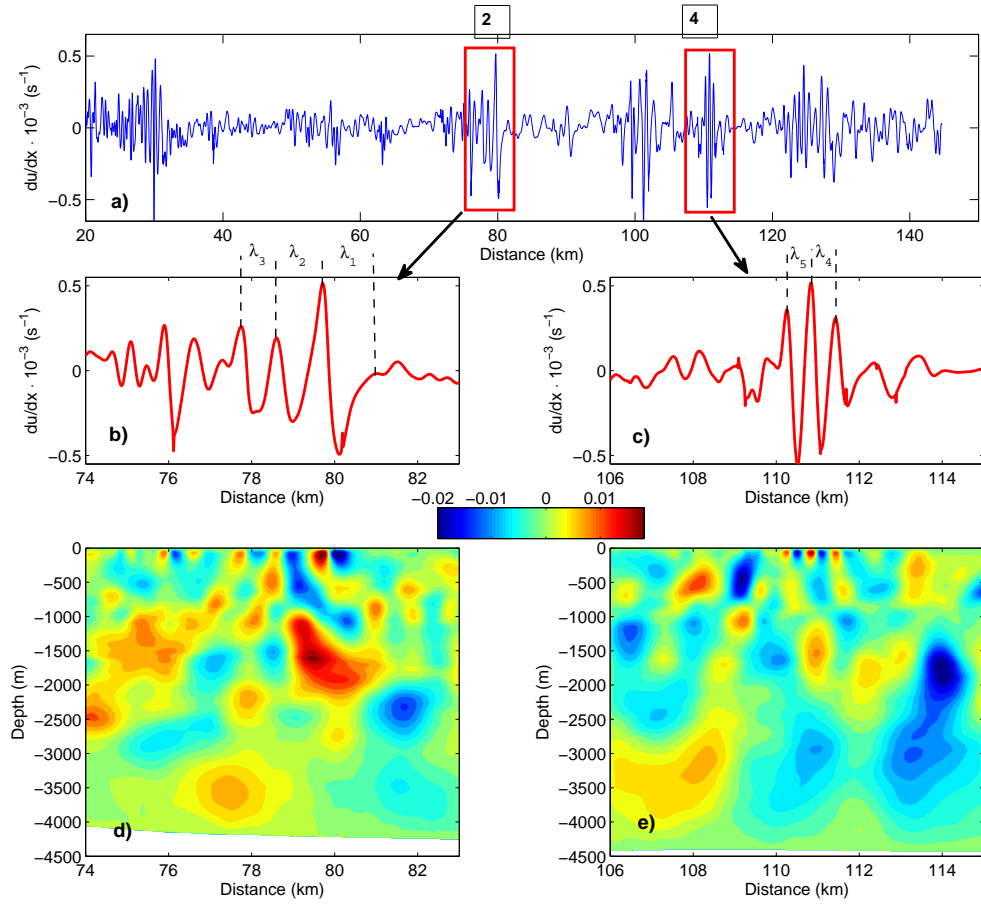
Figure 12: (a) Gradient of the horizontal velocity at the free surface $\partial u/\partial x(z=0)$ after 252 hours of the model run (see bottom line in Fig.11 a). Wave systems (1)-(2) and (3)-(4) in Fig.11 are marked here by red rectangles with numbers 2 and 4, respectively. (b) and (c) Zoom of two fragments shown in panel (a) by red rectangles. (d) and (f) Vertical velocity of the two wave fragments shown in panels (b) and (c).
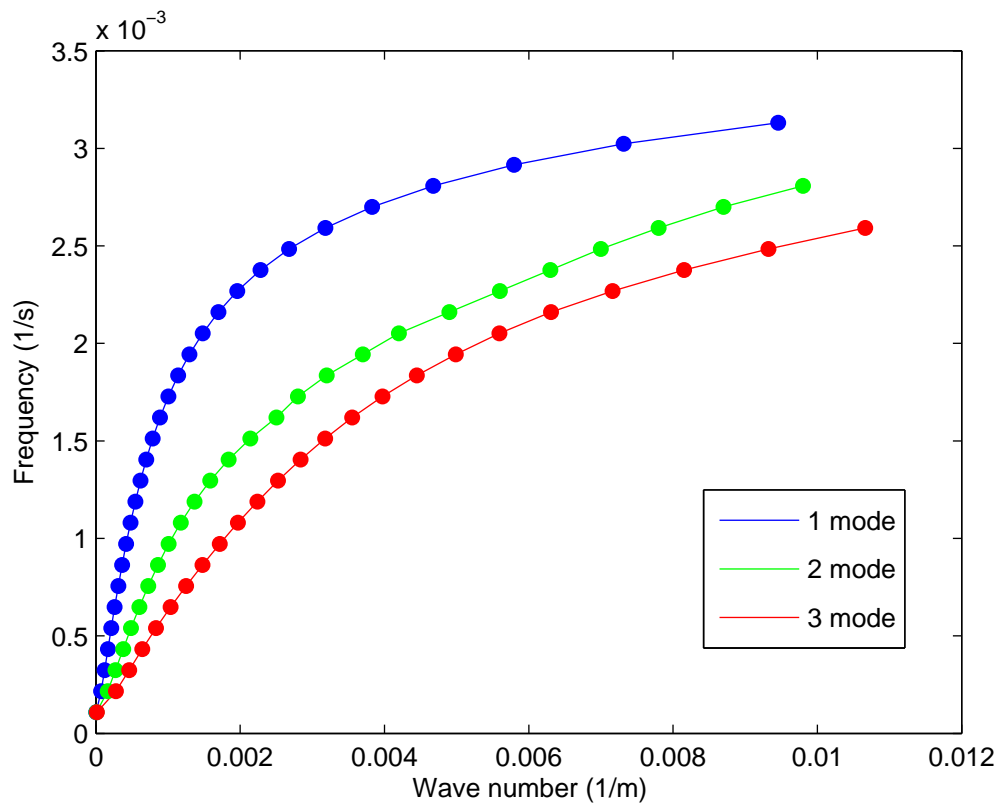
Figure 13: The dispersion relations calculated using the BVP (7) for the first (blue), second (green), and third (red) baroclinic modes.
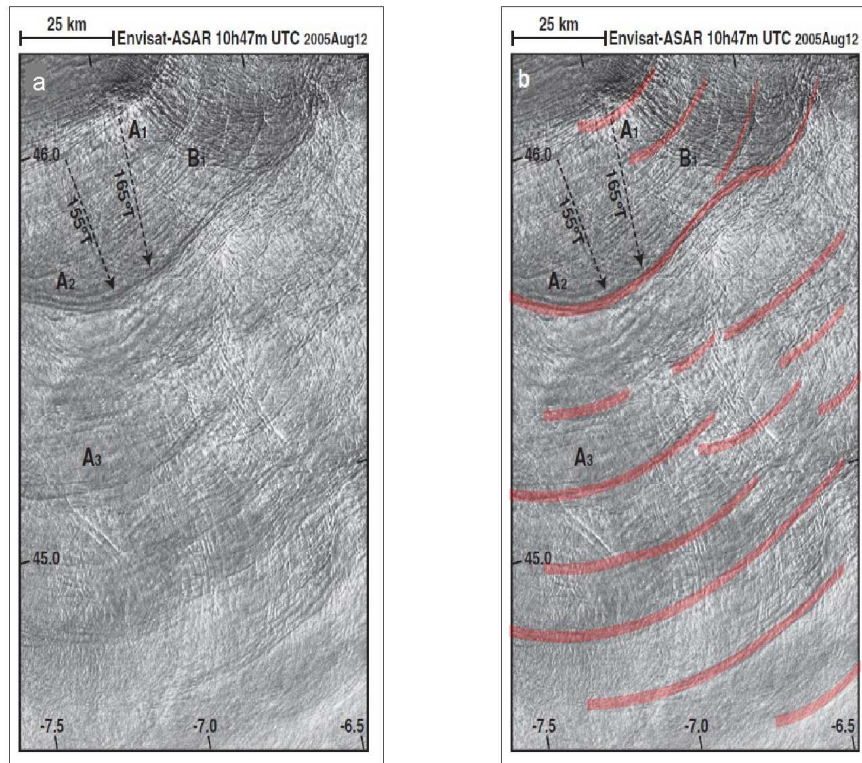
Figure 14: a) Envisat-ASAR image acquired on 12 August 2005 at 10 h 47 m UTC (Muacho et al., 2014). b) The same image with marked by red signatures of ISW packets.